Amylose / cellulose nanofiber composites for all-natural, fully biodegradable and flexible bioplastics

Jinchuan Xu [a,b,*], Domenico Sagnelli [c,*], Marwa Faisal [b], Alixander Perzon [b], Vincenzo Taresco [c], Marco Mais [c], Concetta Valeria L. Giosafatto[d], Kim H. Hebelstrup [e], Peter Ulvskov [b], Bodil Jørgensen [b], Ling Chen [a], Steven M. Howdle [c], Andreas Blennow [b#]

[a] *School of Food Science and Engineering, South China University of Technology, 510640, Guangzhou, China*

[b] *Department of Plant and Environmental Sciences, University of Copenhagen, 1871, Frederiksberg C, Denmark*

[c] *School of Chemistry, University of Nottingham, NG7 2RD, Nottingham, United Kingdom*

[d] *Department of Chemical Science, University of Naples, 80126 Napoli, Italy*

[e] *Department of Molecular Biology and Genetics, Aarhus University, 4200, Slagelse, Denmark*

[#]Corresponding author. E-mail address: abl@plen.ku.dk

[*]The first two authors contributed equally to this work

Abstract: Thermoplastic, polysaccharide-based plastics are environmentally friendly. However, typical shortcomings include lack of water resistance and poor mechanical properties. Nanocomposite manufacturing using pure, highly linear, polysaccharides can overcome such limitations. Cast nanocomposites were fabricated with plant engineered pure amylose (AM), produced in bulk quantity in transgenic barley grain, and cellulose nanofibers (CNF), extracted from agrowaste sugar beet pulp. Morphology, crystallinity, chemical heterogeneity, mechanics, dynamic mechanical, gas and water permeability, and contact angle of the films were investigated. Blending CNF into the AM matrix significantly enhanced the crystallinity, mechanical properties and permeability, whereas glycerol increased elongation at break, mainly by plasticizing the AM. There was significant phase separation between AM and CNF. Dynamic plasticizing and anti-plasticizing effects of both CNF and glycerol were demonstrated by NMR demonstrating high molecular order, but also non-crystalline, and evenly distributed 20 nm-sized glycerol domains. This study demonstrates a new lead in functional polysaccharide-based bioplastic systems.

Keywords: bioplastics; amylose; starch; cellulose nanofibers; composite films

Highlights

- Engineered amylose and waste CNF generate good bioplastics.
- CNF enhanced crystallinity, mechanics and permeability.
- Cellulose nanofibers and amylose showed domain phase separation.

1 Introduction

Increased plastics pollution in the environment has attained notable attention to find alternative eco-friendly and biobased solutions. Such materials refer to renewable resources, preferably of plant-based and waste stream origins that are biodegradable, or home-compostable and non-toxic (Khalil, Bhat & Ireana Yusra, 2012; Mohanty, Misra & Drzal, 2002; Thakur & Thakur, 2015). However, production of such all-natural bioplastics turns out to be challenging and associated problems mainly related to water sensitivity and brittleness (Follain, Joly, Dole & Bliard, 2005; Sagnelli et al., 2016; Sagnelli et al., 2017b).

Starch, the most important energy resource in plants, and cellulose, a main constituent in the plant cell wall, are two of the most abundant carbohydrates in nature providing raw materials for bioplastics production. Starch is an inexpensive, renewable, biodegradable and non-toxic natural polysaccharide (Dai, Zhang & Cheng, 2019; Gross & Kalra, 2002) typically combined of two major polymers, amylose (AM) and amylopectin, which in their native granular form are packed in concentric growth rings forming semi-crystalline and amorphous layers (Copeland, Blazek, Salman & Tang, 2009). AM is an essentially unbranched (approximately 0.1-0.5% branched) polymer composed of α-(1-4)-linked glucose units that contributes mainly to the amorphous phase (Tester, Karkalas & Qi, 2004) while amylopectin has a more branched structure due to additional α-(1-6) branch points (Blennow et al., 2013; Thakur, Pristijono, Scarlett, Bowyer, Singh & Vuong, 2019). Starch is a native

granular assembly structure that is almost fully shattered by hydration during any common manufacturing processes. However, their inherent molecular structures, which differ from one starch type to another, will direct the formation of new diverse semi-crystalline and viscoelastic systems during cooling and aging (Sagnelli et al., 2016). Hence, the semi-crystalline and visco-elastic nature of starch has profound influence on properties and functions of starch-derived bioplastics.

Using pure starch systems as raw material for bioplastics entails drawbacks, such as a poor cohesiveness and brittleness (Follain, Joly, Dole & Bliard, 2005). Usually the brittleness can be overcome adding a plasticizer e.g. glycerol, which offers flexibility and elasticity, reduces brittleness of the material (Giosafatto, Di Pierro, Gunning, Mackie, Porta & Mariniello, 2014) and also maintains biodegradability. Blending starch with glycerol reduces inter- and intra-molecular hydrogen bonding interactions thereby increasing the movement and rearrangnet of the glucan chains. The poor cohesiveness of these films could be overcome by blending with compatible polymers providing an entangled system or grafting or crosslinking the starch with highly flexible polymers.

Starch, even high-AM starch, has a non-optimal structure for entangled matrices due to the presence of highly branched amylopectin providing too short chain segments for stable double-helical junction zones to be formed. AM could not until now be obtained in bulk quantities at reasonable price. However, the production of pure AM in a transgenic barley grain system (Carciofi et al., 2012) has permitted bulk

prodution of AM for e.g. biomaterials purpose. Due mainly to its linear molecular structure, AM is regarded as an optimal raw material for bioplastics purpose (Follain, Joly, Dole & Bliard, 2005) and our previous work has demonstrated that a pure AM can provide significantly improved mechanical strength as compared to normal starch, in extruded materials and its high gelatinization temperature provides high thermal stability comparable to semi-natural bioplastics such as MaterBi® (Sagnelli et al., 2016; Sagnelli et al., 2017a). Biosynthesis directly in the cereal grain can for the first time enable inexpensive bulk production of AM, which hitherto has not been possible due to too high costs for separation of AM from amylopectin.

Blends of AM with other natural biopolymers has the potential to further improve mechanical properties, permeability and thermostability without using artificial or mineral oil-based resources. For example, cellulose is a linear homo-polysaccharide consisting of thousands of β-(1→4)-D-glucopyranose residues. Natural cellulose in plant cell walls is in the form as cellulose microfibrils (3 nm in width and several micrometers long) from several glucopyranose chains, which is a remarkably robust structure that strengthens plant cell walls (McNamara, Morgan & Zimmer, 2015; Somerville et al., 2004). Cellulose nanofibers (CNF) are 5 - 60 nm wide and 0.1 - 2 μm long structures can be derived from plant biomass as first demonstrated by Turbak et al. (Turbak, Snyder & Sandberg, 1983) and Herrick et al. (Herrick, Casebier, Hamilton & Sandberg, 1983). Depending on the pre-treatment method, various types of nano-scale cellulose (nanocellulose) can be obtained.

Nevertheless, CNF is usually preferred as reinforcing agent in composite materials due to its high aspect (length to width) ratio (Klemm et al., 2018; Saïd Azizi Samir, Alloin, Paillet & Dufresne, 2004). Hydrogen-bonding between several neighboring cellulose chains generate densely packed CNF that possess high strength, stiffness, low density and biodegradability (Moon, Martini, Nairn, Simonsen & Youngblood, 2011). Therefore, CNF can be used to improve the mechanical and barrier properties of bio-composites (Vilarinho, Sanches Silva, Vaz & Farinha, 2018). Recently, CNF derived from agricultural side streams consisting mainly of primary cell walls, has generated special interest due to facile and cleaner preparation methods compared to using wood as raw material (Perzon et al., 2019; Holland et al., 2019). Protocols for preparing CNF from vegetable pulp typically consists of alkaline treatment to strip off non-cellulosic polysaccharides, followed by oxidation of phenolic compounds and finally high-shear homogenization. CNF have successfully been derived from sugar beet, potato tuber, and carrot using this method (Dinand, Chanzy & Vignon, 1996; Dufresne, Dupeyre & Vignon, 2000; Siqueira, Oksman, Tadokoro & Mathew, 2016). Indeed, the abundance of pulp originating from industrial production of commodities such as starch, sugar, pectin etc. constitutes a sustainable source of CNF.

Blending starch (but not pure AM) with CNF have demonstrated some superior properties of such blends, possibly partly due to strong interaction between the α- and β-glucosidic polysaccharides. CNF can be extracted from different commodities such as cassava, corn and maize and produced by harsh chemo-physical treatments and

chemical modification (Chen, Liu & Chen, 2019), However, composites of 1:99 ratio CNF:starch suffered from poor dispersion resuling in breaking of the films. Studies on the reinforcement of cassava starch with CNF plasticized with a mixture of sorbitol and glycerol (Teixeira, Pasquini, Curvelo, Corradini, Belgacem & Dufresne, 2009), showed that the elastic modulus increased with 5 wt. % of CNF. However, at 10 and 20 % of CNF, significant reduction in elasticity occurred, suggesting that plasticizer used could delay the stress transfer between the CNF and the matrix.

The present work reports the first attempt of the preparation and characterization of nanocomposite films based on pure AM derived from bioengineered grain, CNF derived from waste sugar beet pulp and glycerol as plasticizer. We hypothesized that pure AM directly derived from a transgenic plant blended with secondary cell wall CNF from waste sugarbeet pulp provides a bulk solution for production of durable AM-based flexible bioplastics. Hence, the main novelty is the use of entirely new raw materials 1. AM directly produced as a virtually pure substance directly in a cereal grain and 2. CNF extracted for pulp providing unique functionality. It is the first time these two raw materials combinedly have been tested for bioplastics purpose. Such AM-CNF cast composite films provided high mechanical stress at break, high Young's modulus, decreased water contact angles and water vapor and oxygen permeability at high CNF content. This study demonstrates some unique properties of nanocomposites fabricated by cast of reinforcing, waste-derived CNF and all-natural bulk-produced AM for biobased bioplastics.

2 Experimental

2.1 Materials

Sugar beet pulp was kindly provided as an agro-industrial side stream by Nordic Sugar A/S. CNF (85%) was extracted as previously described (Perzon et al., 2019). AM (99%) was prepared as described from a starch branching enzyme RNA interference suppressor barley line (Carciofi, Blennow, Nielsen, Holm & Hebelstrup, 2012). All chemicals were provided by Sigma-Aldrich (St. Louis, MO, USA).

2.2 Methods

2.2.1 Extraction of AM

Barley flour was mixed at a ratio of 1:10 with a solution containing 1 mM dithiotreitol (DTT) and 0.5% SDS (sodium dodecyl sulphate). The suspension was homogenized at 5700 rpm using a Silverson L5A homogenizer with the largest slit size for 10 min and then at 8300 rpm for 20 min. The AM granules were sedimented at 4 ºC over night or until the supernatant was visually clear. The supernatant was carefully discarded, and the AM-containing sediment washed with MilliQ water three times and sieved through a 100 μm mesh. The AM was collected and washed again with MilliQ water. A white layer consisting of AM granules (Figure S1) was collected and dried at room temperature. Purity and molecular characteristics are documented elsewhere (Shaik et al., 2014,2016; Goldstein et al., 2016).

2.2.2 Gelatinisation profile of AM

To establish the dissolution characteristics of amylose at thos conditions (high temperature) as the dissolution method used to produce the bioplastics films, the gelatinisation profile of AM was monitored using a rheometer (Anton Paar, Ireland, MCR102) equipped with a leak-proof pressure cell and a Rapid Visco Analyzer (RVA) vane geometry (Anton Paar, Ireland, ST24-4V-2D). A 10% w/w suspension of AM was prepared in triplicate. The experiment was performed using the following program: mixing at 960 rpm for 90 s at 50 °C, pasting at 170 rpm, by a temperature ramp from 50 °C to 145 °C at a rate of 2 °C/min, an isotherm at 145 °C for 30 min, a cooling ramp from 145 °C to 50 °C at a rate of 3 °C/min.

2.2.3 Extraction of cellulose nanofibers

Cellulose nanofibers were prepared from sugar beet pulp as described elsewhere (Perzon et al., 2019). Briefly, 20 g (dry weight) of sugar beet was added to 2500 mL distilled water (dH_2O) and homogenized to pulp (particle sizes around 1 mm) with a Silverson L5A homogenizer (East Longmeadow, MA, USA) at 5600 rpm for 10 min and thereafter at 8300 rpm for 20 min using a slotted disintegrating head. The pulp was subsequently washed with 5000 mL of dH_2O though a 38 μm sieve and then suspended in 500 mL 0.5 M NaOH, stirred at 80 ºC for 2 h, and washed until neutral with dH_2O. To remove lignin and tannins, the NaOH-treated pulp was submerged in 500 mL bleach solution (1% $NaClO_2$ and pH 5.0), stirred at 70 ºC for 2 h, and washed

192 with dH_2O. After obtaining the dry weight of the remaining suspension of cellulose
193 fibers, it was diluted to 1.00% (w/w) in 200 mL dH_2O. The cellulose fibers (200 mL)
194 were circulated in a high-shear homogenizer (microfluidizer materials processor
195 M110-P, Newton, MA, USA) with orifices of 200 and 400 μm under 500 bar pressure
196 for 18 min to produce nanofibers. The nanofibers were stored at 4 °C until further use
197 (Figure S1).
198
199 *2.2.4 Casting of composites films*
200 The different nanocomposite formulations of AM and CNF with different
201 glycerol content were prepared as previously published with minor modification
202 (Sagnelli et al., 2017b). The CNF:AM were 0:100, 25:75, 50:50, 100:0 (w/w %). All
203 constituents (1% each of CNF and AM and different glycerol concentrations) were
204 heated while stirring for 30 min at 140 ºC using a high-pressure glass reactor. The
205 solutions were cooled to approximately 70 ºC, degassed in vacuum and immediately
206 cast in Teflon-coated petri dishes. The films were dried at 50 ºC in a ventilated oven
207 overnight or until completely dry and transparent (Figure S2). All the samples are
208 named to indicate the percentages of the different components where CNF and AM
209 constitutes 100% and the amounts of glycerol indicated additionally, as for example
210 15/25/75 for a sample containing 15 % glycerol, 25% CNF and 75% AM. All pure
211 components and composite films were placed in a sealed desiccator containing
212 saturated potassium chloride (RH 85, 20 ºC) to balance the moisture before analysis.

213

214 *2.2.5 Confocal Laser Scanning Microscopy (CLSM)*

215 The films were analyzed by CLSM (Leica SP5-X, Leica Microsystems, IL,
216 USA) equipped with x20 water immersion objectives. Pontamine Fast Scarlet 4BS
217 (PFS 4BS) and safranin O (Sigma-Aldrich) were used as fluorophores for CNF and
218 AM, respectively. The excitation fluorescence were 488 nm and 488 nm and emitted
219 fluorescence were recorded between 560 - 605 nm and 530 - 550 nm, respectively, for
220 PFS and safranin O. Images analysis was performed with LAS AF X 2.6 software
221 (Leica Microsystems, IL, USA).

222

223 *2.2.6 Field Emission Scanning Electron Microscopy (FE-SEM)*

224 FE-SEM images were acquired with a Quanta 3D FEG (FEI Company, The
225 Netherlands). The films were cut into squares (1 × 1 cm), attached to a metal plate,
226 and coated with a 2 nm colloidal gold layer before analysis. The cross section
227 morphology, film specimens were cryo-fractured by immersion in liquid nitrogen and
228 then mounted on aluminum stubs perpendicularly to their surface then sputtered with
229 gold prior to analysis.

230

231 *2.2.7 Water contact angles (Θw)*

232 Water contact angles (Θw) of films were performed at room temperature with a
233 KSV Cam 200 (KSV Instruments Ltd, Helsinki, Finland). Measurments the were
234 performed after 10 sec from the contact to the film and no variation was recorded after
235 that time. Left and right values were recorded and an average was calculated. Angle

pictures were recorded by using the built-in software (CAM200, KSV instruments). All measurements were recorded in duplicates.

2.2.8 Attenuated total reflectance Fourier-transform infrared (ATR-FTIR) spectroscopy

ATR-FTIR spectra were acquired with an attenuated total reflection spectrophotometer (Agilent Technologies Cary 630 FTIR, Santa Clara CA, USA) equipped with reflection ATR unit. Spectra were acquired with a resolution of 4 cm^{-1}, in the range 4000 - 650 cm^{-1} by acquiring 32 interferograms. Spectra were analyzed with the open access software SpectraGryph1.2.

2.2.9 Wide angle X-ray scattering (WAXS)

Following moisture equlilibration (RH 85, 20 ^{o}C) collection of data was performed using a Panalytical Xpert Pro (Nottingham, UK) instrument. The samples were tested in the WAXS (wide-angle X-ray scattering) mode and the intensity given according to $q = 4\pi \sin\theta/\lambda$, where λ is the wavelength and 2θ is the scattering angle set from 5° to 35°. The exposure time was 400 s/step with a step increment of (0.0131303°) (Sagnelli et al., 2019). For calculation of the crystallinity, the peak analyser tool of Origin2020b PRO was used. In particular a baseline was obtained to remove the amorphous phase to consider only the crystalline phase. Peaks were fitted and integrated to obtain the crystalline contribution. The total area (amorphous +

crystalline) was measured following integration the whole spectra. Subtraction between the integrated areas provided the amorphous contribution.

2.2.10 Mechanical properties

The films were cut into rectangular strips of length = 100 mm and width = 8 mm, Film thickness, as measured by a micrometer screw gauge, varied as a function of the composition. The tensile tests were performed using an Instron machine model 5569 (MTS, USA) equipped with a 5 kN tensile load cell. The distance between clamps was 60 mm and the crosshead speed were set at 10 mm min^{-1}. The elongation and tensile stress at break were measured at 18 °C and 50% humidity. Each analysis was performed at least in pentaplicate (Follain, Joly, Dole & Bliard, 2005). Young´s modulus was calculated as follows: E=FL0/ADL. with F = force L0 Length A= thickness DL= difference between L0 and Lfin (Lfin the length before the deformation starts.

2.2.11 Dynamic mechanical analysis with temperature and humidity control

Dynamic mechanical analysis (DMA, Triton technology, 2101405) with a temperature gradient was performed in tension mode with a displacement of 0.005 mm and frequencies of 1 and 10 Hz. A standard heating rate of 3 °C min^{-1} was used and a ramp from −50 to 120 °C. The experiments were performed on prototypes with a length of 10 mm. The glass transition temperature was estimated by comparing the

derivative function of the storage modulus and the tan delta (tanδ) peak (Sagnelli et al., 2019; Figure S3).

2.2.12 Nuclear magnetic resonance magic-angle spinning (NMR MAS)

Conventional solid-state NMR MAS experiments on ^{1}H were performed on a Bruker Avance III 600 MHz spectrometer, equipped with a triple resonance 1.3 mm fast-MAS (magic angle spinning) probe operating at ambient temperature. Zirconia rotors were used for all experiments, and spinning frequencies were set to 60.0 kHz and regulated to ± 2 Hz. ^{1}H chemical shifts were referenced externally to the ^{1}H resonances of adamantane set at 1.8 ppm. Relaxation times were measured by using a standard saturation recovery sequence, consisting in a saturation block of multiple 90° pulses, followed by an increasing recovery time and a final 90° and acquisition. One-dimensional ^{1}H spectra were acquired with the use of a spin-echo sequence in order to remove the background signal from the probe. It consisted in a 90° - delay –180° sequence and the signal is detected after a second echo delay. Ultrafast magic angle spinning ^{1}H – ^{1}H two-dimensional exchange spectra were recorded with increasing mixing times, and the changes in peak intensities were used to monitor the transfer of magnetization between the domains by spin diffusion. The sequence used was a standard NOESY sequence, suitable for identifying signals from protons in close proximity (Jennings et al., 2016; Ntountaniotis et al., 2014).

2.2.13 Permeability to gases

Water vapor permeability (WVP), carbon dioxide (CO_2) and oxygen (O_2) permeabilities were evaluated as described (Mariniello, Giosafatto, Di Pierro, Sorrentino & Porta, 2010; Sagnelli et al., 2017b). The films were placed in a desiccator for two days at 85 % RH in order to secure that all the samples reached the same level of humidity since also water may act as plasticizer and therefore may influence the barrier properties. The films were cut into 5 cm^2 squares and the experiment was performed at 25 °C under 85% RH in duplicate.

3 Results and discussion

3.1 Solubilisation profile of AM

Prior to the production of the bio-nanocomposites, the solubilisation behavior of AM in a high-pressure rheometer was tested. We recorded three different solubilisation transitions for 10% w/w AM/water suspensions. The first transition was detected at 87 ℃, indicating that the granules were starting to swell and take up water (Fig. 1). The main transition was detected at 97 °C indicating the solubilisation and gelatinization of the granules (Fig. 1). The last transition was detected at 140 °C showing the solubilisation of AM/lipid complexes (Fig. 1). These data agree with solubilisation profiles for AM measured by differential scanning calorimetry (Sagnelli et al., 2016). As guided by the last transition, we set the temperature for gelatinization of the AM in the suspensions to 140 °C to secure complete dissolution of all crystallites prior of the casting phase.

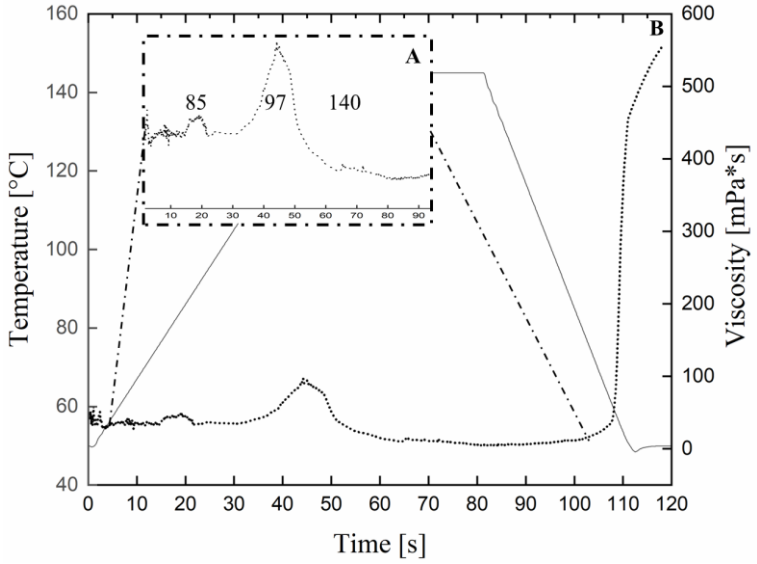

Fig. 1. Gelatinization profile of 10% AM suspensions recorded in an air-tight high-pressure cell. A: the main gelatinization transitions. B Gelation phase.

3.2 Surface and internal structures of films

FE-SEM surface analysis of films produced from AM and CNF specimens at different ratios showed that the topography and the cross section changed significantly with increasing CNF content. Additional detailed information of the surface alterations as compared to previous studies on composite CNF starch systems [35-37] were revealed. The 0/0/100 (pure AM) film surface showed numerous pleated structures (Fig. 2a). CNF blended to 25 % resulted in a smoother surface indicating an interaction between the two polysaccharides where the CNF are located internally and coated by AM (Fig. 2b). When CNF content was raised to 50 % and 100 % fiber-like structures became visible on the surface of the films (Fig. 2c, d). The films plasticized with glycerol showed no significant differences as compared to the non-plasticized films (not shown). The coating of the nanofibers with the starch matrix indicate that the nanofibers were physically reinforced in the network, which demonstrates that the two polymers are compatible. No voids or pores were observed in the film, which indicated

a strong adhesion between the nanofibers and the starch successively reinforcing the matrix and enhancing the mechanical strength.

FE-SEM images of the cross section of cryo-fractured surfaces of the composite films (Fig. 2) showed that the pure AM film presented a smooth dense fractured surface that is typical of a brittle material (Fig. 2e). High homogenous distribution of CNF at 25%, which lead to strong interfacial adhesion (Fig. 2f). Both surface and cross section became more non-homogeneous with increased concentration of CNF to 50% that revealing low interfacial adhesion between nanofibers and matrix (Fig. 2g). The pure CNF film showed uniform layers of fibers (Fig. 2h). Only few cracks and deformations within the starch matrix indicates even distribution of the polymeric structures in the matrix.

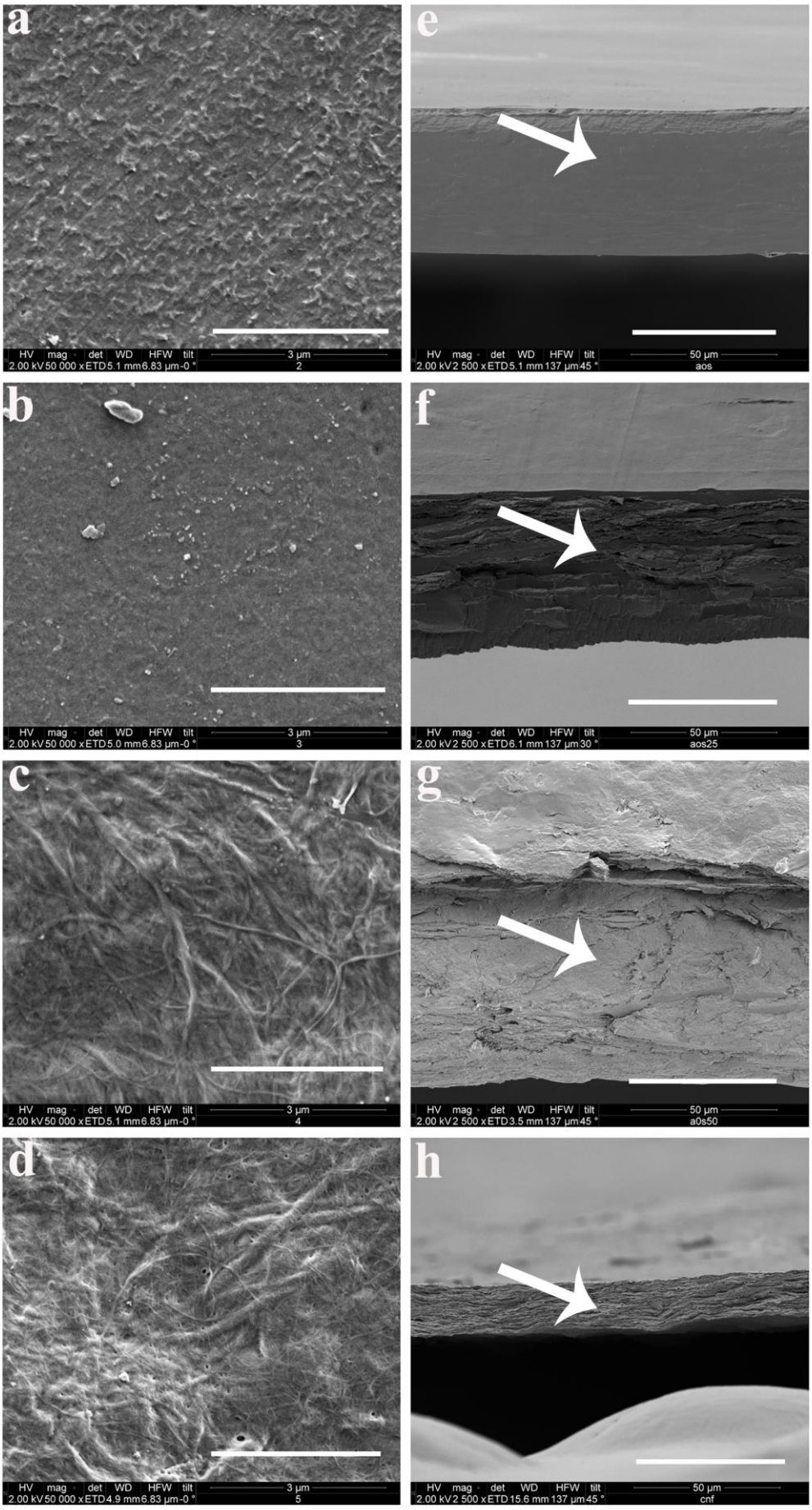
a
HV mag det WD HFW tilt
2.00 kV 50 000 x ETD 5.1 mm 6.83 µm -0 °
3 µm
2
e
HV mag det WD HFW tilt
2.00 kV 2 500 x ETD 5.1 mm 137 µm 45 °
50 µm
aos
b
HV mag det WD HFW tilt
2.00 kV 50 000 x ETD 5.0 mm 6.83 µm -0 °
3 µm
3
f
HV mag det WD HFW tilt
2.00 kV 2 500 x ETD 6.1 mm 137 µm 30 °
50 µm
aos25
c
HV mag det WD HFW tilt
2.00 kV 50 000 x ETD 5.1 mm 6.83 µm -0 °
3 µm
4
g
HV mag det WD HFW tilt
2.00 kV 2 500 x ETD 3.5 mm 137 µm 45 °
50 µm
a0s50
d
HV mag det WD HFW tilt
2.00 kV 50 000 x ETD 4.9 mm 6.83 µm -0 °
3 µm
5
h
HV mag det WD HFW tilt
2.00 kV 2 500 x ETD 15.6 mm 137 µm 45 °
50 µm
cnf

352

Fig. 2. FE-SEM of AM/CNF pure and composite films. (a,e) surface and cross section for 0/0/100; (b,f) surface and cross section for 0/25/75; (c,g) surface and cross section for 0/50/50; (d,h) surface and cross section for 0/100/0. Arrows indicate fissure surfaces. Scale bars represent 3μm for the surfaces (left) and 50 μm for the cross sections (right).

The internal structure of the films was analyzed by CLSM (Chen, Yu, Simon, Petinakis, Dean & Chen, 2009) using two different fluorophores, safranin O and PFS 4BS (Anderson, Carroll, Akhmetova & Somerville, 2010; Dürrenberger, Handschin, Conde-Petit & Escher, 2001) permitting identification of AM and cellulose domains, respectively (Fig. 3). The pure AM and CNF films displayed virtually homogeneous internal phases as evaluated by the safranin O and PFS 4BS staining, respectively. No cross-contamination with AM or cellulose of these pure films was detected as deduced from the virtual absence of green fluorescence in the pure AM system and very little red fluorescence in the pure CNF system. Phase partitioning between CNF and AM was readily detected in the 0/25/75 and 0/50/50 films as separated bright and dark fields representing safranin O-stained AM and PFS 4BS stained CNF domains. These results clearly suggest a partial phase separation between AM and CNF. The same phenomenon was observed for nanocomposites of starch and betaglucans (Sagnelli et al., 2017b). Phase separation can be an effect of the slow fabrication

(casting) process and not due to the special features of the AM and CNF used in the study as compared to other similar raw materials.

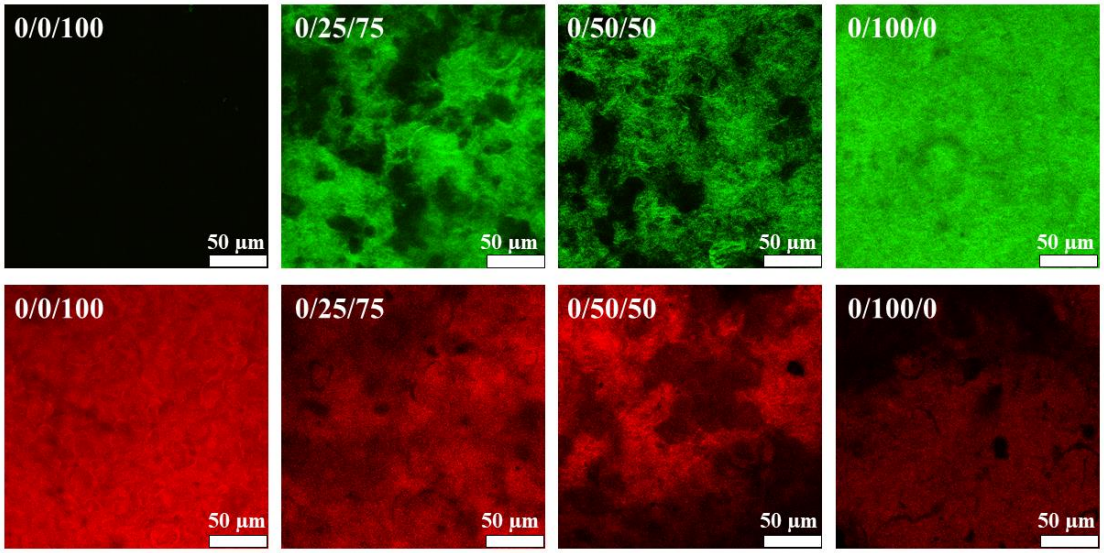

Fig. 3. CLSM images of AM/CNF pure and composite films. Green flourescence of CNF with PFS 4BS; the dark areas of composites identify AM. Red staining of AM with safranin O; the dark areas of composites identify CNF domains. Scale bars: 50 µm.

3.3 Water contact angles of films

The water contact angle (Θ_w) is defined as the angle formed by the intersection of the tangent lines of the liquid and surfaces of the solid at the three-phase boundary (generally liquid, solid and air) (Wong, Gastineau, Gregorski, Tillin & Pavlath, 1992). The water contact angle provides information related to the degree of hydrophilic/hydrophobic nature of a surface, and is indicative of the surface wettability as well as the strength of the molecular interaction among liquid, solid, and

air phases (Gutiérrez, Ollier & Alvarez, 2018). The water contact angle increases with increased surface hydrophobicity. Polysaccharides typically show relatively high $\Theta_{w,}$ which is suggested to be related to strong intermolecular hydrogen bonding among the hydroxyl groups of the polysaccharide backbone with the surface of films (Karbowiak, Debeaufort, Champion & Voilley, 2006; Ojagh, Rezaei, Razavi & Hosseini, 2010).

The Θ_w values of the composite films were affected in various degrees by the AM:CNF ratios and glycerol (Table 1). Without glycerol, CNF decreased the Θ_w value suggesting strong positive effect of CNF on the surface wettability. The water contact angles of 0/50/50 and 0/100/0 were lower than 65°, indicating the CNF decreased intermolecular hydrogen bonding in the polysaccharide composite matrix. Pure AM and 0/25/75 (75% AM) films showed water contact angles $\geqslant 65^{\circ}$ suggesting low wettability of these composites. Addition of 15% glycerol to the AM film showed little effect. However, when both CNF and glycerol were included, the water contact angle increased, suggesting glycerol-induced increase in intramolecular bonding in the composite.

With a high (25%) glycerol concentration, the AM films showed a notable increase in Θ_w suggesting the presence of strong intermolecular hydrogen bonding between glycerol and AM in the AM matrix and the presence of specific AM-glycerol structures (Karbowiak, Debeaufort, Champion & Voilley, 2006). On the other hand, high glycerol concentration in the AM/CNF composites showed a significant

411 variability in Θ_w. Among the 25% glycerol samples, we observed an unexpectedly
412 low contact angle (46°) for the 25% glycerol sample (25/25/75, Table 1), which we
413 suggest is due to a decrease of the intermolecular hydrogen bonding network. These
414 effects could not be readily explained and might be caused by a wide variety of
415 different amorphous and crystalline phases in the films. Especially, glycerol, due to
416 the anti-plasticizing effect of the glycerol, may affect the distribution of AM and CNF
417 in the films, inducing formation of aggregates at the surface of films leading to
418 increased water contact angles.
419
420 Table 1. The moisture, crystallinity and contact angle of AM/CNF pure and composite
421 films.

Composition	Moisture (%)	Crystallinity (%)	Contact angle (degrees)
0/0/100	12.08	14	87.0±1.0
0/25/75	13.67	18	67.0±1.0
0/50/50	9.58	23	58.0±1.0
0/100/0	7.23	40	55.0±1.0
15/0/100	12.87	15	90.0±1.0
15/25/75	16.15	12	87.0±1.0
15/50/50	13.12	34	74.0±1.0
15/100/0	14.74	57	81.0±1.0

25/0/100	15.83	18	111.0±1.0
25/25/75	12.41	20	46.0±1.0
25/50/50	15.56	43	100.0±1.0
25/100/0	14.34	55	60.0±1.0

422

423 *3.4 Fourier-transform infrared spectroscopy (FTIR)*

424 FTIR was conducted in order to test if new chemical bonds or physical
425 interactions (mainly H-bonding) were formed during the processes. The ATR FTIR
426 spectra (Figure S4) showed O–H stretching, corresponding to a broad band between
427 3600 - 3200 cm^{-1}, due to an extensive H-bonding network among the OH of AM
428 glycerol and cellulose. The C–H stretching was observed at 2900 cm^{-1}. The
429 appearance of an absorption band at 1650 cm^{-1} is attributed to the water adsorbed, due
430 to the hygroscopic nature of polysaccharides. The peaks at 1050 to 950 cm^{-1}, related
431 to the C–O–C stretching showed a slight shift towards higher wave number for the
432 CNF-containing films demonstrating an additive effect of CNF. Otherwise, all the
433 spectra were very similar and hence, we conclude that no new covalent bonds formed
434 between AM and CNF, as previously reported for CNF-starch composites (Liu &
435 Budtova, 2012). As deduced from FTIR glycerol had only minor effects on the
436 bonding network of the films (Figure S4).

437

3.5 Crystalline structures

AM/CNF pure and composite films were found to possess well-defined crystalline structures as deduced by wide angle X-ray scattering (WAXS) (Table 1 and Fig. 4). The AM films exhibited a typical V-type polymorph mainly formed by single-helices (Xu, Tan, Chen, Li & Xie, 2019) as demonstrated by diffraction peaks at 2θ of 5.5°, 16.0°, 17.0° and 20.0°. CNF film displayed characteristic diffraction peaks at 2θ of 16.2° and 22.3°, which represent a typical Type-I crystalline structure (Lu, Lin, Tang, Wang, Chen & Huang, 2015), showing that the purification and melt processing of CNF had little effects on its crystalline structures. The crystallinity of the films increased with CNF content. Interestingly, the diffractograms did not seem to be entirely additive for AM and CNF and for the 50% and 100% CNF the cellulose crystalline polymorph dominated as were virtually the same indicating very amorphous AM. Glycerol did not have any significant effect on crystallinity for any of the film formulations except for the 50% CNF, which had an unexpectedly high crystallinity (Table 1). A 2-fold higher crystallinity as compared to the films without glycerol was found indicating that glycerol has weaker interaction with CNF than with AM creating an imbalance in the composites when the amount of CNF exceed a certain limit. This can increase the relative amount of glycerol interacting with the AM-phase of the nanocomposite allowing more moisture absorption and the overall crystallinity. This was confirmed by the small change of crystallinity for pure CNF

458 films and by the water contact angle of 50/% CNF films that does not follow the trend
459 when 25% of glycerol was added.

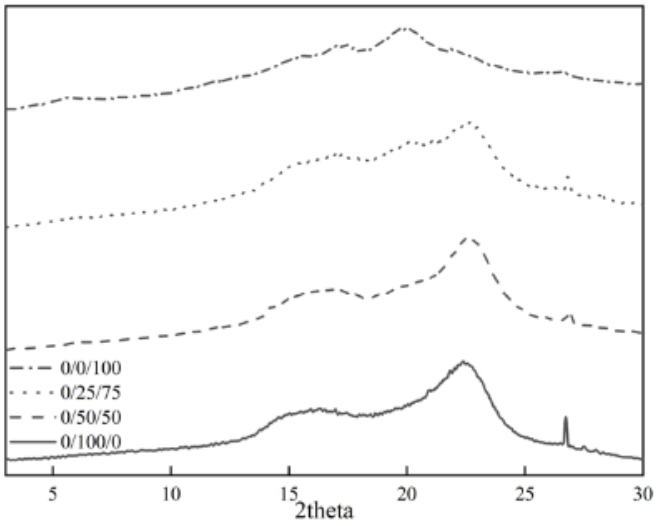

460

461 Fig. 4. WAXS diffractograms of AM/CNF pure and composite films without glycerol.

462

463 *3.6 Mechanical properties*

464 The deformation behavior of AM/CNF pure and composite films as
465 characterized by tensile tests and calculation of the parameters strain at break, stress at
466 break and Young's modulus showed that the films were influenced by all three
467 components AM, CNF and glycerol (Fig. 5). The presence of glycerol decreased the
468 stiffness and strength of the films and increased elasticity. In particular, when we
469 intended to plasticize the AM films with 15 % of glycerol an anti-plasticization effect
470 was observed as demonstrated by decreased strain at break. This effect has been
471 previously recorded for thermoplastic starch (TPS) materials (Lourdin, Bizot &
472 Colonna, 1997). Interestingly, the addition of 25 % CNF reverted the anti-
473 plasticization showing a 5-fold increase in the strain at break, which is a typical effect

for nanocomposites. The strain at break decreased with increased CNF and for the pure CNF, strain at break increased only 2-fold confirming the lower affinity of CNF to glycerol. At higher concentration of glycerol, the strain at break increased significantly with the concentration of CNF in the composites.

Increased CNF:AM ratio resulted in higher stress at break for the films without glycerol, demonstrating that CNF had a significant strengthening effect on the composites. In the presence of glycerol there was a drop in the strength of all the films (Fig. 5B). At 15% glycerol, the stress at break of the samples was not significantly different for any of the films. However, the Young´s modulus of these films increased with increasing CNF content. When glycerol content was increased to 25%, the strength of AM and composites films showed a notable decrease. However, the pure CNF films showed indifferent strength, virtually independent of the glycerol content demonstrating that CNF has a great potential as filler and reinforcer. As deduced from the combined high stress and strain at break, the CNF films showed high cohesiveness even with high concentration of glycerol.

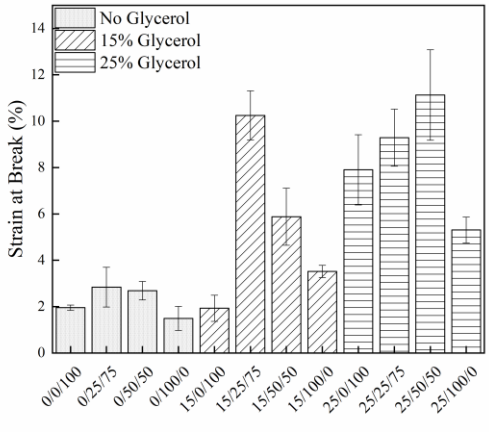

490

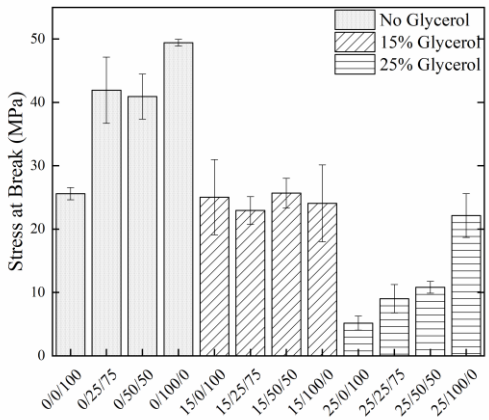

491

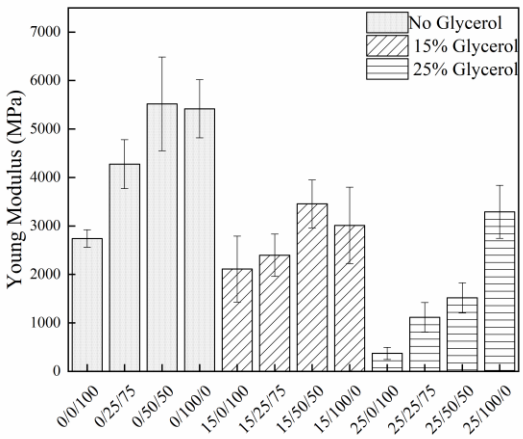

492

493 Fig. 5. Mechanical properties of AM/CNF pure and composite films. Top: strain at

494 break, Middle: stress at break, Bottom: Young's modulus.

495

3.7 Effects of temperature on dynamic visco-elasticity

The visco-elastic properties of the films were analyzed with a dynamic mechanical analyzer (DMA) using tension mode and temperature gradients to estimate the glass transition temperature and calculating the tanδ peak (Sagnelli et al., 2017b). There was a general trend that the presence of CNF and glycerol decreased the T_g of the films (Figure S5). However, just as shown for the strain at break, a weak anti-plasticization effect was observed at 15% glycerol for the films with high AM content. This effect has been previously recorded for high AM films (Lourdin, Bizot & Colonna, 1997). Generally, at 25% glycerol T_g was decreased demonstrating a notable plasticized system where the polymers chains have flexibility in the plasticizer-rich phases.

3.8 Solid-state NMR

Solid-state NMR spectroscopy was used to evaluate the domain size of the different component on the whole sample. ^{1}H ultrafast-MAS solid-state NMR experiments were performed on AM/CNF pure and composite films. NMR relaxation measurements are sensitive to the crystalline nature of the materials, high degree of crystallinity induce a strong network of dipole-dipole interactions which results in fast spin-lattice relaxation times (T_1). Relaxation was monitored over a range of 100 s for each sample and the extracted relaxation times were fast (order of magnitude of a few seconds) and characterized by a mono-exponential behavior. This, together with the fact that all the chemical sites show the same relaxation behavior, suggests that the

domains present in the composites were relatively small (nm scale) and intimately distributed. The relaxation times decreased with the increase of the glycerol content of the films. Moreover, the relaxation times decreased as CNF was increased in the films and this effect was most noticeable in absence of glycerol (Fig. 6). The addition of glycerol substantially modified the relaxation behaviour of all the films by decreasing the relaxation, compatible with a plasticizing effect of the glycerol.

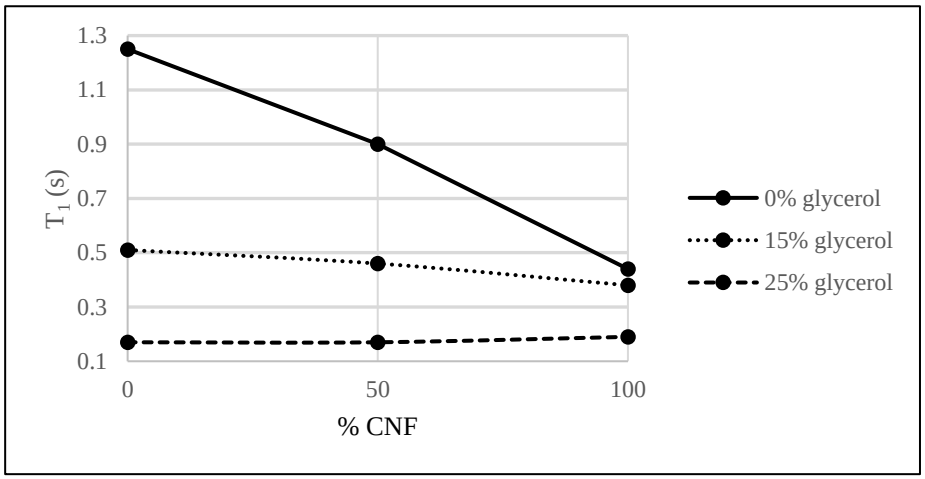

Fig. 6. 1H Spin-lattice relaxation times as a function of CNF and glycerol contents.

Ultrafast-MAS ^{1}H spin-echo experiments were performed at 60.0 kHz to characterize the chemical environments of the films. All the spectra show an aliphatic region between 0 and 2 ppm indicating small amount of impurities. Spectra for the films without glycerol were not resolved enough to differentiate between the different chemical sites. Even though the resolution did not fully resolve each chemical environment of the protons it was clear that AM showed a spectrum with a relative sharp peak centered at approx. 4 ppm, characterized by two small shoulders, one at

3.5 ppm and the second one at approximately 6.0 ppm (Fig. 7A). The CNF spectrum instead showed only one broad resonance at 4 ppm. However, the lack of resolution for the pure spectra makes the structural analysis and the peak assignment impossible. On the other hand, the effect of the addition of glycerol (Fig. 7B,C,D) is easily noticeable by the appearance of two sharp and intense glycerol resonances, at 3.7 and 4.8 ppm respectively, which substantially overlapped with the AM/CNF unresolved protons.

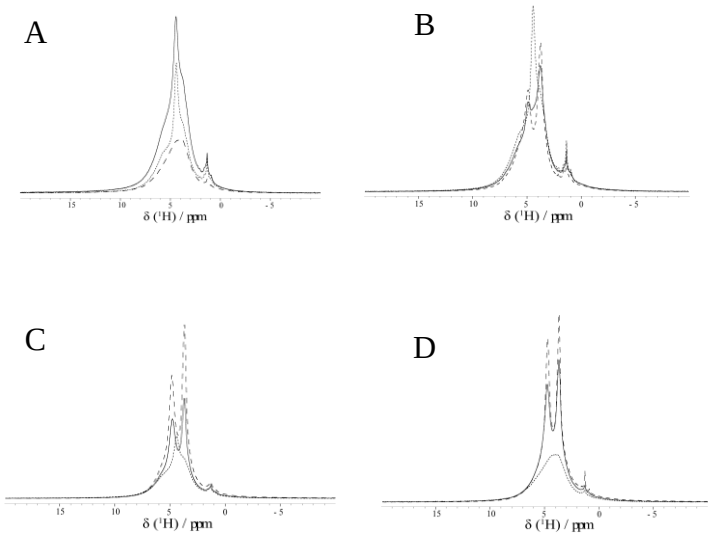

Fig. 7. 1H solid-state NMR MAS Hahn-echo spectra. A: 0/0/100 (dotted line), 0/50/50 (solid line) and 0/100/0 (dashed line); B: 0/0/100 (dotted line), 15/0/100 (solid line) and 25/0/100 (dashed line); C: 0/50/50 (dotted line), 15/50/50 (solid line) and 25/50/50 (dashed line); D: 0/100/0 (dotted line), 15/100/0 (solid line) and 25/100/0 (dashed line).

To obtain additional data on the average domain size, solid-state NMR $^{1}H - {}^{1}H$ spin diffusion measurements were carried out. The NOESY proton-exchange experiment (Fig. 8), performed at a different mixing times in the range 1 to 300 ms, showed the presence of cross-peaks demonstrating that there is a substantial fast magnetization exchange transferring the polarization between the different domains of the matrix. This suggests that the relative domain size in the samples are small, which is compatible with the previous observation that only a single mono-exponential relaxation behavior is present for all peaks. However, since the glycerol signals obscure the AM/CNF chemical shifts and due to the similarity of the two pure AM and CNF films, calculation of the copolymeric blocks are not precise. However, from the resolved glycerol peak signal it is possible to estimate the upper limit for the glycerol domain size according to (Pili et al., 2018) $< r^2 > = 6Dt$, setting the spin diffusion coefficient to the order of magnitude of 10^{-16} m^2s^{-1} and t to T_1, an upper limit of 20 nm can be assumed for the domain size of the glycerol. These data are compatible with the CLSM results (Fig. 3) in which the phase separation involves only AM and cellulose.

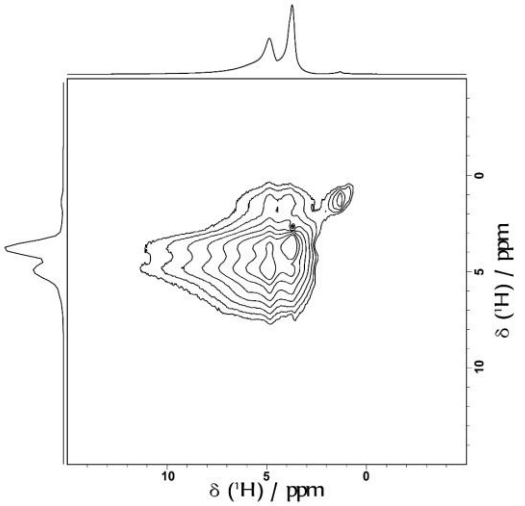

Fig. 8. 1H - 1H NOESY exchange for the 25/100/0 sample.

3.9 Gas permeability

Water vapor (WVP), carbon dioxide (CO_2) and oxygen (O_2) permeability measurements were carried out on films without glycerol (Table 2). AM films (0/0/100) were too fragile to be tested for O_2 and CO_2. WVP decreased with increased CNF; the pure AM films showed a 7-fold higher WVP than the CNF films. Such effects have been discussed (Ferrer et al. , 2017) in terms of the dense network structure that is formed by CNF as we documented by SEM providing a more tortuous diffusion path for gases. Furthermore, the WVP of all the composite films were far lower than the majority of petroleum-based materials (Ferrer, Pal & Hubbe, 2017). The same effects of CNF were seen for O_2 and CO_2, especially for the O_2 permeability showing a 3-fold decrease as compared to the AM-rich composites. The reduced O_2 permeability can be advantageous for packaging purposes.

583

584 Table 2. Barrier properties of AM/CNF pure and composite films.

Composition	Thickness (μm)	Permeability (cm^3 mm kPa/m^2 24h)		
		O_2	CO_2	H_2O
0/0/100	66±2	ND*	ND*	0.351±0.020
0/25/75	47±4	13.0 ±3	0.14±0.05	0.059±0.007
0/50/50	68±2	4.2±2.6	11±0.5	0.056±0.001
0/100/0	43±2	3.1±0.1	1.83±0.01	0.057±0.009

585 * Not determined due to fragility.

586

587 ## 4 Conclusions

588 Composite transparent films were fabricated by casting of pure plant engineered
589 AM from transgenic barley grain and waste-derived primary cell wall CNF. The
590 presence of 25% CNF resulted in a smooth composite while increased CNF had
591 rougher surface, fiber-like surface structures and increased wettability. Phase
592 partitioning between AM and CNF was identified using CLSM indicating only partial
593 interaction between the two polymers. Crystallinity, mechanical strength and stiffness
594 were increased by CNF. All composites showed increased elasticity (strain at break)
595 as compared to the pure polysaccharide prototypes demonstrating that even minor
596 AM-CNF interactions have major effect on mechanical properties. An anti-
597 plasticizing effect in the AM film was observed at 15% glycerol but this was reversed

598 in the presence of 25% CNF. Solid-state NMR relaxation times were suppressed by
599 both CNF and glycerol demonstrating plasticizing effects of these constituents. Spin-
600 echo ^{1}H data substantiated the presence of high molecular, but non-crystalline,
601 ordered domains in the AM matrix. The glycerol domains within the pure and
602 composite films were in the range of 20 nm and distributed in close proximity to each
603 other. The permeability to O_2 and water were substantially reduced with increasing
604 concentration of CNF. This study demonstrate novel agrowaste and plant engineered
605 polysaccharide raw materials for the development of all-natural and fully home-
606 compostable composite blends as an alternative to (partially) synthetic bioplastics to
607 reduce plastics pollution.
608

609 ## Acknowledgements

610 This research was funded by Danish council for independent research (grants
611 number 7026-00060B and 8022-00095B) and China Scholarship Council (CSC,
612 201806150107). The work presented here was partly supported by the Innovation
613 Foundation Denmark with the Project 5152− 00001B; Assembly: Reverse engineering
614 the cell wall for high performance Bio composites. We also thank The Center for
615 Advanced Bioimaging, Faculty of Science, the University of Copenhagen.
616

617 ## Supplementary Material

618 Figure S1. FE-SEM images of AM granules (A, B) and CNF (C, D)

Figure S2. Transparency of films.

Figure S3. Evaluation of the storage modulus by the first derivative and the TanDelta peak.

Figure S4. AT FTIR spectra of AM/CNF pure and composite films in the region 4000 - 650 cm^{-1}.

Figure S5. Glass transition (Tg) temperatures of pure and composite films as deduced from DMA.

References

Anderson, C. T., Carroll, A., Akhmetova, L., & Somerville, C. (2010). Real-time imaging of cellulose reorientation during cell wall expansion in Arabidopsis roots. *Plant Physiol*, *152*(2), 787-796.

Blennow, A., Jensen, S. L., Shaik, S. S., Skryhan, K., Carciofi, M., Holm, P. B., Hebelstrup, K. H., & Tanackovic, V. (2013). Future cereal starch bioengineering: cereal ancestors encounter gene technology and designer enzymes. *Cereal Chemistry*, *90*(4), 274-287.

Carciofi, M., Blennow, A., Jensen, S. L., Shaik, S. S., Henriksen, A., Buléon, A., Holm, P. B., & Hebelstrup, K. H. (2012). Concerted suppression of all starch branching enzyme genes in barley produces amylose-only starch granules. *BMC Plant Biology*, *12*(1), 223.

Carciofi, M., Blennow, A., Nielsen, M. M., Holm, P. B., & Hebelstrup, K. H. (2012). Barley callus: a model system for bioengineering of starch in cereals. *Plant Methods*, *8*(1).

639 Chen, P., Yu, L., Simon, G., Petinakis, E., Dean, K., & Chen, L. (2009). Morphologies and
640 microstructures of cornstarches with different amylose–amylopectin ratios studied by confocal
641 laser scanning microscope. *Journal of Cereal Science, 50*(2), 241-247.
642 Chen, Q., Liu, Y., & Chen, G. (2019). A comparative study on the starch-based biocomposite
643 films reinforced by nanocellulose prepared from different non-wood fibers. *Cellulose, 26*(4),
644 2425-2435.
645 Copeland, L., Blazek, J., Salman, H., & Tang, M. C. (2009). Form and functionality of starch.
646 *Food Hydrocolloids, 23*(6), 1527-1534.
647 Dai, L., Zhang, J., & Cheng, F. (2019). Effects of starches from different botanical sources and
648 modification methods on physicochemical properties of starch-based edible films. *International*
649 *Journal of Biological Macromolecules, 132*, 897-905.
650 Dinand, E., Chanzy, H., & Vignon, M. (1996). Parenchymal cell cellulose from sugar beet pulp:
651 preparation and properties. *Cellulose, 3*(1), 183-188.
652 Dufresne, A., Dupeyre, D., & Vignon, M. R. (2000). Cellulose microfibrils from potato tuber
653 cells: processing and characterization of starch–cellulose microfibril composites. *Journal of*
654 *Applied Polymer Science, 76*(14), 2080-2092.
655 Dürrenberger, M. B., Handschin, S., Conde-Petit, B., & Escher, F. (2001). Visualization of
656 Food Structure by Confocal Laser Scanning Microscopy (CLSM). *LWT - Food Science and*
657 *Technology, 34*(1), 11-17.
658 Ferrer, A., Pal, L., & Hubbe, M. (2017). Nanocellulose in packaging: Advances in barrier layer
659 technologies. *Industrial Crops and Products, 95*, 574-582.

660 Follain, N., Joly, C., Dole, P., & Bliard, C. (2005). Mechanical properties of starch-based
661 materials. I. Short review and complementary experimental analysis. *Journal of Applied*
662 *Polymer Science, 97*(5), 1783-1794.
663 Giosafatto, C. V., Di Pierro, P., Gunning, P., Mackie, A., Porta, R., & Mariniello, L. (2014).
664 Characterization of Citrus pectin edible films containing transglutaminase-modified phaseolin.
665 *Carbohydr Polymers, 106*, 200-208.
666 Goldstein, A., Annor, G., Putaux, J. L., Hebelstrup, K. H., Blennow, A., Bertoft, E (2016).
667 Impact of full range of amylose contents on the architecture of starch granules. *International*
668 *Journal of Biological Macromolecules*, 89, 305–318.
669 Gross, R. A., & Kalra, B. (2002). Biodegradable Polymers for the Environment. *Science*,
670 *297*(5582), 803-807.
671 Gutiérrez, T. J., Ollier, R., & Alvarez, V. A. (2018). Surface Properties of Thermoplastic Starch
672 Materials Reinforced with Natural Fillers. 131-158.
673 Herrick, F. W., Casebier, R. L., Hamilton, J. K., & Sandberg, K. R. (1983). Microfibrillated
674 cellulose: morphology and accessibility. *Journal of Applied Polymer Science: Appl. Polym.*
675 *Symp.;(United States)* (Vol. 37): ITT Rayonier Inc., Shelton, WA.
676 Holland, C., Perzon, A., Cassland, P. R. C., Jensen, J. P., Langebeck, B., Sorensen, O. B.,
677 Whale, E., Hepworth, D., Plaice-Inglis, R., Moestrup, O., Ulvskov, P., & Jorgensen, B.
678 (2019). Nanofibers produced from agro-industrial plant waste using entirely enzymatic
679 pretreatments. *Biomacromolecules*, 20(1), 443-453

Jennings, J., Bassett, S., Hermida-Merino, D., Portale, G., Bras, W., Knight, L., Titman, J. J., Higuchi, T., Jinnai, H., & Howdle, S. (2016). How does dense phase CO 2 influence the phase behaviour of block copolymers synthesised by dispersion polymerisation? *Polymer Chemistry*, *7*(4), 905-916.

Khalil, H. P. S. A., Bhat, A. H., & Ireana Yusra, A. F. (2012). Green composites from sustainable cellulose nanofibrils: A review. *Carbohydrate Polymers, 87*(2), 963-979.

Karbowiak, T., Debeaufort, F., Champion, D., & Voilley, A. (2006). Wetting properties at the surface of iota-carrageenan-based edible films. *Journal of Colloid Interface Science, 294*(2), 400-410.

Klemm, D., Cranston, E. D., Fischer, D., Gama, M., Kedzior, S. A., Kralisch, D., Kramer, F., Kondo, T., Lindström, T., & Nietzsche, S. (2018). Nanocellulose as a natural source for groundbreaking applications in materials science: Today's state. *Materials Today*.

Liu, W., & Budtova, T. (2012). Ionic liquid: A powerful solvent for homogeneous starch–cellulose mixing and making films with tuned morphology. *Polymer, 53*(25), 5779-5787.

Lourdin, D., Bizot, H., & Colonna, P. (1997). "Antiplasticization" in starch-glycerol films? *Journal of Applied Polymer Science, 63*(8), 1047-1053.

Lu, Q., Lin, W., Tang, L., Wang, S., Chen, X., & Huang, B. (2015). A mechanochemical approach to manufacturing bamboo cellulose nanocrystals. *Journal of Materials Science, 50*(2), 611-619.

699 Mariniello, L., Giosafatto, C. V. L., Di Pierro, P., Sorrentino, A., & Porta, R. (2010). Swelling,
700 Mechanical, and Barrier Properties of Albedo-Based Films Prepared in the Presence of
701 Phaseolin Cross-Linked or Not by Transglutaminase. *Biomacromolecules, 11*(9), 2394-2398.
702 McNamara, J. T., Morgan, J. L., & Zimmer, J. (2015). A molecular description of cellulose
703 biosynthesis. *Annual review of Biochemistry, 84*, 895-921.
704 Mohanty, A. K., Misra, M., & Drzal, L. T. (2002). Sustainable Bio-Composites from
705 Renewable Resources: Opportunities and Challenges in the Green Materials World. *Journal of*
706 *Polymers and the Environment, 10*(1), 19-26.
707 Moon, R. J., Martini, A., Nairn, J., Simonsen, J., & Youngblood, J. (2011). Cellulose
708 nanomaterials review: structure, properties and nanocomposites. *Chemical Society Reviews,*
709 *40*(7), 3941-3994.
710 Ntountaniotis, D., Kellici, T., Tzakos, A., Kolokotroni, P., Tselios, T., Becker-Baldus, J.,
711 Glaubitz, C., Lin, S., Makriyannis, A., & Mavromoustakos, T. (2014). The application of solid-
712 state NMR spectroscopy to study candesartan cilexetil (TCV-116) membrane interactions.
713 Comparative study with the AT1R antagonist drug olmesartan. *Biochimica et Biophysica Acta*
714 *(BBA)-Biomembranes, 1838*(10), 2439-2450.
715 Ojagh, S. M., Rezaei, M., Razavi, S. H., & Hosseini, S. M. H. (2010). Development and
716 evaluation of a novel biodegradable film made from chitosan and cinnamon essential oil with
717 low affinity toward water. *Food Chemistry, 122*(1), 161-166.

718 Perzon, A., Jørgensen, B., & Ulvskov, P. (2019). Sustainable production of cellulose nanofiber
719 gels and paper from sugar beet waste using enzymatic pe-treatment. *Carbohydrate Polymers*,
720 115581.
721 Pili, S., Rought, P., Kolokolov, D. I., Lin, L., Da Silva, I., Cheng, Y., Marsh, C., Silverwood, I.
722 P., García Sakai, V., & Li, M. (2018). Enhancement of Proton Conductivity in Nonporous
723 Metal–Organic Frameworks: The Role of Framework Proton Density and Humidity. *Chemistry*
724 *of Materials*, *30*(21), 7593-7602.
725 Reddy, N., & Yang, Y. (2010). Citric acid cross-linking of starch films. *Food Chemistry*, *118*(3),
726 702-711.
727 Sagnelli, D., Cavanagh, R., Xu, J., Swainson, S. M. E., Blennow, A., Duncan, J., Taresco, V.,
728 & Howdle, S. (2019). Starch/Poly (Glycerol-Adipate) Nanocomposite Film as Novel
729 Biocompatible Materials. *Coatings*, *9*(8), 482.
730 Sagnelli, D., Hebelstrup, K. H., Leroy, E., Rolland-Sabate, A., Guilois, S., Kirkensgaard, J. J.
731 K., Mortensen, K., Lourdin, D., & Blennow, A. (2016). Plant-crafted starches for bioplastics
732 production. *Carbohydr Polymers*, *152*, 398-408.
733 Sagnelli, D., Hooshmand, K., Kemmer, G. C., Kirkensgaard, J. J. K., Mortensen, K., Giosafatto,
734 C. V. L., Holse, M., Hebelstrup, K. H., Bao, J., Stelte, W., Bjerre, A. B., & Blennow, A. (2017a).
735 Cross-Linked Amylose Bio-Plastic: A Transgenic-Based Compostable Plastic Alternative.
736 *International Journal of Molecular Science* , *18*(10).

737 Sagnelli, D., Kirkensgaard, J. J. K., Giosafatto, C. V. L., Ogrodowicz, N., Kruczala, K.,
738 Mikkelsen, M. S., Maigret, J. E., Lourdin, D., Mortensen, K., & Blennow, A. (2017b). All-
739 natural bio-plastics using starch-betaglucan composites. *Carbohydr Polymers, 172*, 237-245.
740 Saïd Azizi Samir, M. A., Alloin, F., Paillet, M., & Dufresne, A. (2004). Tangling effect in
741 fibrillated cellulose reinforced nanocomposites. *Macromolecules, 37*(11), 4313-4316.
742 Savadekar, N. R., & Mhaske, S. T. (2012). Synthesis of nano cellulose fibers and effect on
743 thermoplastics starch based films. *Carbohydrate Polymers, 89*(1), 146-151.
744 Shaik., S.S ., Carciofi, M., Martens, H.J., Hebelstrup, K. H., and Blennow, A. (2014). Starch
745 bioengineering affects cereal grain germination and seedling establishment. *Journal of*
746 *Experimental Botany*, 65/9, 2257–2270.
747 Shaik, S.S., Obata, T., Hebelstrup, K. H., Fernie, A. R., Mateiu, R.V., Blennow, A. (2016).
748 Starch granule re-structuring by starch branching enzyme and glucan water dikinase modulation
749 affects caryopsis physiology and metabolism. *PLoS ONE* 11(2): e0149613.
750 Siqueira, G., Oksman, K., Tadokoro, S. K., & Mathew, A. P. (2016). Re-dispersible carrot
751 nanofibers with high mechanical properties and reinforcing capacity for use in composite
752 materials. *Composites Science and Technology, 123*, 49-56.
753 Somerville, C., Bauer, S., Brininstool, G., Facette, M., Hamann, T., Milne, J., Osborne, E.,
754 Paredez, A., Persson, S., & Raab, T. (2004). Toward a systems approach to understanding plant
755 cell walls. *Science, 306*(5705), 2206-2211.

Teixeira, E. d. M., Pasquini, D., Curvelo, A. A. S., Corradini, E., Belgacem, M. N., & Dufresne, A. (2009). Cassava bagasse cellulose nanofibrils reinforced thermoplastic cassava starch. *Carbohydrate Polymers, 78*(3), 422-431.

Tester, R. F., Karkalas, J., & Qi, X. (2004). Starch—composition, fine structure and architecture. *Journal of Cereal Science, 39*(2), 151-165.

Thakur, R., Pristijono, P., Scarlett, C. J., Bowyer, M., Singh, S. P., & Vuong, Q. V. (2019). Starch-based films: Major factors affecting their properties. *International Journal of Biological Macromolecules, 132,* 1079-1089.

Thakur, V. K., & Thakur, M. K. (2015). Recent advances in green hydrogels from lignin: a review. *International Journal of Biological Macromolecules, 72*, 834-847.

Tomé, L. C., Fernandes, S. C. M., Perez, D. S., Sadocco, P., Silvestre, A. J. D., Neto, C. P., Marrucho, I. M., & Freire, C. S. R. (2013). The role of nanocellulose fibers, starch and chitosan on multipolysaccharide based films. *Cellulose, 20*(4), 1807-1818.

Turbak, A. F., Snyder, F. W., & Sandberg, K. R. (1983). Microfibrillated cellulose, a new cellulose product: properties, uses, and commercial potential. *J. Appl. Polym. Sci.: Appl. Polym. Symp.;(United States)* (Vol. 37): ITT Rayonier Inc., Shelton, WA.

Vilarinho, F., Sanches Silva, A., Vaz, M. F., & Farinha, J. P. (2018). Nanocellulose in green food packaging. *Critical Reviews in Food Science and Nutrition, 58*(9), 1526-1537.

Vogler, E. A. (1998). Structure and reactivity of water at biomaterial surfaces. *Advances in Colloid and Interface Science, 74*(1), 69-117.

776 Wong, D. W., Gastineau, F. A., Gregorski, K. S., Tillin, S. J., & Pavlath, A. E. (1992). Chitosan-
777 lipid films: microstructure and surface energy. *Journal of Agricultural and Food Chemistry*,
778 *40*(4), 540-544.
779 Xu, J., Tan, X., Chen, L., Li, X., & Xie, F. (2019). Starch/microcrystalline cellulose hybrid gels
780 as gastric-floating drug delivery systems. *Carbohydr Polymers*, *215*, 151-159.
781